
**MULTIPARTICLE PROBLEMS OF QUANTUM OPTICS
AND QUANTUM INFORMATICS**

Quantum Many-Body Simulations Using Gaussian Phase-Space Representations¹

P. D. Drummond, P. Deuar, and J. F. Corney

ARC Centre of Excellence for Quantum Atom Optics, University of Queensland, Brisbane, Queensland, Australia

Received October 12, 2006

Abstract—Phase-space representations are of increasing importance as a viable and successful means to study exponentially complex quantum many-body systems from first principles. This paper traces the background of these methods, starting from the early work of Wigner, Glauber and Sudarshan. We focus on modern phase-space approaches using non-classical phase-space representations. These lead to the Gaussian representation, which unifies bosonic and fermionic phase-space. Examples treated include quantum solitons in optical fibers, colliding Bose–Einstein condensates, and strongly correlated fermions on lattices.

PACS numbers: 42.50.Lc

DOI: 10.1134/S0030400X07070028

INTRODUCTION

In this paper, we will trace how the concept of coherence and coherent states has led an important advance: the quantum phase-space representation. Through the development of phase-space representations, the idea of coherence can help the understanding and simulation of the physics of many-body systems, both in thermal equilibrium, and in time-dependent, quantum dynamical calculations. This is of increasing importance beyond quantum optics, as new experiments explore the quantum correlations and dynamics of interacting particles.

We show that a more general approach to coherence leads to the Gaussian phase-space method, which unifies the representation of both bosonic and fermionic many-body systems. This powerful idea has many ramifications. It encompasses all the known bosonic representations in a simple, clear formalism, and extends these ideas to fermions as well. It is also extremely useful in applications, as we will show using both equilibrium and non-equilibrium examples.

A particular quantum state that illustrates this is the coherent state. It was introduced originally by Schrödinger [1] for the harmonic oscillator, and later applied to the radiation field through the seminal work of Sudarshan [2] and Glauber [3]. These states are fully coherent in the sense that normally ordered operator moments factorize to all orders.

The definition of a coherent state is extremely simple. If \hat{a} is a field-mode annihilation operator, then the coherent state is defined as a normalized eigenstate of \hat{a} ,

$$\hat{a}|\alpha\rangle = \alpha|\alpha\rangle. \quad (1)$$

These states form a complete mathematical basis, providing examples of quantum states which are perfectly coherent to all orders. The idea can be extended to other algebras, for example the $SU(N)$ coherent states, and were used to construct the P -representation—a representation of the radiation field in terms of diagonal coherent state projection operators. This *quantum operator representation* has the form (for a single mode) of

$$\hat{\rho} = \int P(\alpha)|\alpha\rangle\langle\alpha|d^2\alpha. \quad (2)$$

This representation maps a quantum state into a distribution on a classical phase space. Other representations like this exist, including the Wigner [4] representation and the Husimi [5] Q -function. The closely related operator associations of Lax [6], Agarwal [7, 8] and co-workers were used to develop a quantum theory of the laser. While useful for the laser, these all lack essential ingredients that would allow them to be useful as a probability distributions in first-principles many-body dynamical simulations. Most are simply non-positive, as in the case of the P -function and Wigner function. Any representation that uses a classical-like phase space has no corresponding exact stochastic equation when there are inter-particle interactions.

We will explain how this problem is solved by extending the phase-space dimension, giving rise to the positive P -representation [9, 10]. A unifying principle is the use of non-orthogonal basis sets, which leads to the idea of a stochastic gauge symmetry [11], and more general Gaussian phase-space methods [12, 13]. These have many applications to interacting Bose and Fermi systems. Both thermal equilibrium and first-principles quantum dynamical time-evolution (either unitary or dissipative) can be treated. Recent bosonic examples include quantitatively tested predictions on quantum

¹ The text was submitted by the authors in English.

soliton time-evolution [14], as well as novel predictions for topical experiments including: colliding Bose-Einstein condensates [15], tunnel-coupled condensates [16], superchemistry [17], molecular dissociation [18–21], micro-mechanical resonators [22], triple EPR correlations [23], and non-equilibrium criticality in parametric downconversion [24]. We also give results for phase-space simulations of the fermionic Hubbard model in thermal equilibrium [25].

QUANTUM MANY-BODY SYSTEMS

Quantum many-body theory is the generic theory we currently use for describing all non-astronomical physical systems from a microscopic point of view. It is applicable to a wide range of problems.

Ultra-Cold Atomic Gases

As simple examples of interacting quantum systems, consider the ultra-cold atomic Bose-Einstein condensates and degenerate atomic Fermi gases. Ultra-cold atoms are an ideal quantum many-body system. In these experiments, the interacting atoms are isolated from other matter, by virtue of being optically or magnetically trapped in a high-vacuum environment at low temperatures. Important advances in the last decade include: Bose-Einstein condensation (BEC), atom lasers, superfluid Fermi atoms, superchemistry (stimulated molecule formation), atomic diffraction, interferometers, and temperatures below 1 nK.

Such well-controlled and simple physical systems present an opportunity to quantitatively test quantum mechanics in new regimes, where macroscopic and many-body effects play a dominant role.

Many-Body Quantum Dynamics

Before one can make quantitative predictions, there is a significant problem to overcome: quantum many-body problems are exponentially complex.

To illustrate this, consider a Bose gas with N atoms distributed among M modes. Each mode can have one or all atoms. The number N_s of quantum states available is:

$$N_s = \frac{(N + M - 1)!}{N!(M - 1)!}. \quad (3)$$

A typical BEC may have $N \approx M \approx 500000$, giving the astronomical number of

$$N_s = 2^{2N} = 10^{300000}. \quad (4)$$

Hilbert space dimension can also be classified by the number of equivalent quantum bits (qubits), which is $\log_2 N_s = 2N = 1000000$, in this example.

There are a number of possible solutions to dynamical problems. Here we focus on methods which are exact, in the sense that errors can be estimated and

reduced where necessary. As an example, while Density Matrix Renormalisation Group (DMRG) methods [26] can be useful for one-dimensional calculations, including dynamics, the Hilbert-space truncation is not always a well-controlled approximation. Similar difficulties occur in the density functional approach [27]. Uncontrolled approximations cannot be used as a basis for *testing* quantum mechanics. Any discrepancies observed may simply be caused by calculation errors, rather than fundamental issues.

Candidates for *exact* solutions are as follows:

Path integrals and Monte-Carlo—these are useful for bosons at thermal equilibrium. For quantum dynamics and for fermions, there are phase and sign problems, making these methods often impractical.

Perturbation theory—while applicable for certain problems, this method generally doesn't converge in quantum field theory.

Numerical diagonalization—the problem of an exponentially large matrix size rules out such brute force methods, except for very small particle numbers.

Exact solutions—even if all the energy eigenstates are known (which is unusual) evaluating the initial expansion coefficients for quantum dynamics remains exponentially difficult, and therefore impractical.

New hardware—Feynman proposed quantum computers to solve many-body problems—currently, these do *not* exist beyond 2–4 qubit capacity.

New software—*Gaussian quantum phase-space simulation methods can give practical techniques using existing computers, simulating quantum systems equivalent to nearly a million qubits.*

QUANTUM PHASE-SPACE METHODS

The great power of phase-space methods is their ability to accurately compute the quantum dynamics of fully macroscopic systems directly from the Hamiltonian, without resorting to overarching approximations. This confers several advantages over previous methods, despite the introduction of randomness that limits precision:

Firstly, all uncertainty in the results is confined to random statistical fluctuations, with no systematic bias. Importantly, the magnitude of this uncertainty can be reliably estimated from the distribution of sub-ensemble means by using the central limit theorem.

Secondly, these methods lead to relatively simple equations that can be easily adapted to trap potentials and local losses, whose magnitude and shape can be chosen arbitrarily. This is in stark contrast to approximate methods, which can become much more complicated or even inapplicable under such conditions.

The Gaussian quantum phase-space representation described here encompass all the earlier known phase-space methods. Therefore, we start by reviewing these earlier approaches.

Classical and Quantum Phase Space

Wigner [4] originated the idea of a classical-like phase-space or quasi-probability description. For M modes, these methods scale linearly with mode number, having just M complex dimensions. Variations on this theme include the Husimi Q -function [5], and the Glauber-Sudarshan [2, 3] P -representation. For many quantum states, they result in a positive-valued distribution. For the Q -function, this is always true. Despite this, one finds that there is no corresponding stochastic equation for cubic or quartic Hamiltonians. Thus, there is no method for efficiently time-evolving a sampled distribution of an interacting system, except through an approximate truncation of the equations of motion.

The solution to this problem is to use an enlarged phase space, which includes off-diagonal terms in a coherent-state expansion. Intuitively, this allows for quantum superpositions between more than one classical configuration. The simplest possibility is the positive- P ($+P$) distribution [10], which has $2M$ coordinates. It results in a distribution function which is always positive, and given certain conditions, obeys a stochastic equation. It has the definition that

$$\hat{\rho} = \int P(\alpha, \beta) \frac{|\alpha\rangle\langle\beta^*|}{\langle\beta^*|\alpha\rangle} d^2\alpha d^2\beta. \quad (5)$$

Quantum Phase-Space Representations

Guided by the formalism of Eqs. (2) and (5), one can define a general quantum phase-space representation by expanding the density matrix $\hat{\rho}$ using a complete basis of operators $\hat{\Lambda}(\vec{\lambda})$:

$$\hat{\rho} = \int P(\vec{\lambda}) \hat{\Lambda}(\vec{\lambda}) d\vec{\lambda}. \quad (6)$$

Provided $P(\vec{\lambda})$ remains positive and sufficiently bounded, quantum dynamics can be transformed into trajectories in $\vec{\lambda}$. Different basis choices for $\hat{\Lambda}(\vec{\lambda})$ then result in different representations. For example, the P -representation has a single complex dimension (for $M = 1$), so $\lambda_1 = \alpha$, and:

$$\hat{\Lambda}(\alpha) = |\alpha\rangle\langle\alpha|. \quad (7)$$

As shown in Fig. 1, there are trade-offs in the choice of basis, since the quantum variance is partly due to the distribution, and partly due to the basis. By minimizing the distribution variance, one can reduce the sampling error of the representation. This typically involves an over-complete, non-orthogonal basis in which each member of the basis is closely matched to a physical state that occurs in the simulation.

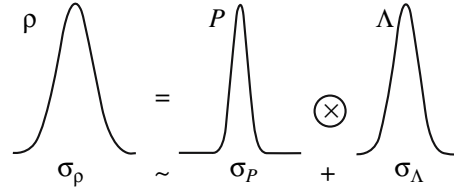


Fig. 1. The full variance σ_ρ is composed of a distribution variance σ_P , and a basis variance σ_Λ .

Fermionic Phase Space

Coherent states for fermions [28, 29] can be defined by means of anti-commuting Grassmann numbers, and have been used, for example, in path-integral formulations for fermions [30]. Like their bosonic counterparts, fermionic coherent states provide an overcomplete basis set, and as Cahill and Glauber showed, can be used to defined phase-space representations for fermions [31]. Unlike their bosonic counterparts, the fermionic coherent states have no direct physical meaning. Moreover, while they are useful for formal calculations, they have limited applicability as a basis for practical, numerical calculations, because of the complexity that arises from the anticommuting properties of the algebra [32]. The coherent-state P -representation is then a function of Grassmann numbers, not a probability.

But this anticommuting complexity is related to the unphysical states contained in the coherent basis. Fermionic coherent states require Grassmann numbers because of the way they include coherences between states with an odd number difference. Consider a coherent superposition of zero and one-particle states: $|\psi\rangle = \alpha|0\rangle + \beta|1\rangle$, which gives a nonzero value for the coherence $\langle a \rangle = \alpha^*\beta$. Because the state $|1\rangle$ involves an anti-commuting operator, one of the amplitudes must also be anticommuting, for consistency. This also means that the coherent amplitude is anticommuting.

However, from superselection rules, we know that fermions can only be created in pairs, and thus such superpositions are excluded. Thus one can avoid this anticommuting problem by considering an operator basis which only includes coherences that are allowed by the superselection rule.

General M -mode Gaussian Operator

The most general phase-space representation, for both fermions and bosons, is obtained with Gaussian operators. These provide an (over) complete basis for fermions even when the coherences, and thus Grassmann components are excluded [33]. These also generalize the concept of coherence: physical states with Gaussian density operators have operator products that factorize in a similar, but more general way than coherent states.

To define these, we introduce $\hat{\mathbf{a}}$ as a column vector of M bosonic/fermionic annihilation operators (indi-

cated as the upper or lower sign respectively), and $\hat{\mathbf{a}}^\dagger$ the corresponding row vector of creation operators. Their commutation relations are

$$[\hat{a}_k, \hat{a}_j^\dagger]_{\mp} = \delta_{kj}. \quad (8)$$

A Gaussian operator is defined as a normally ordered exponential of a quadratic form in annihilation and creation operators. Introducing extended $2M$ -vectors of operators: $\hat{\underline{a}} = (\hat{\mathbf{a}}, (\hat{\mathbf{a}}^\dagger)^T)$, with adjoint defined as $\hat{\underline{a}}^\dagger = (\hat{\mathbf{a}}^\dagger, \hat{\mathbf{a}}^T)$, the operator fluctuation is then: $\delta\hat{\underline{a}} = \hat{\underline{a}} - \underline{\alpha}$, where $\underline{\alpha} = (\boldsymbol{\alpha}, \boldsymbol{\beta}^*)$ is a $2M$ -vector c -number. A Gaussian operator can therefore be written as:

$$\hat{\Lambda}_{\pm} = \Omega |\underline{\underline{\sigma}}|^{\mp 1/2} : \exp \left[\delta\hat{\underline{a}}^\dagger \left(\underline{\underline{I}}_f - \frac{1}{2} \underline{\underline{\sigma}}^{-1} \right) \delta\hat{\underline{a}} \right] : . \quad (9)$$

In the fermionic case the square root of the determinant (for normalization purposes) is to be interpreted as the Pfaffian of the matrix, in an explicitly antisymmetric form. The additional factor $\underline{\underline{I}}$ in the exponent only appears in the fermionic case:

$$\underline{\underline{I}} \equiv \begin{bmatrix} \pm I & 0 \\ 0 & I \end{bmatrix}. \quad (10)$$

Operator Mappings

The covariance $\underline{\underline{\sigma}}$ is best thought of as a kind of dynamical Green's function. It can be expanded as:

$$\underline{\underline{\sigma}} = \begin{bmatrix} \pm \tilde{n}^T & m \\ m^+ & \tilde{n} \end{bmatrix}. \quad (11)$$

Here n is a complex matrix whose average is the normal Green's function for particles, while $\tilde{n} \equiv \mathbf{1} \pm n$. In many-body terminology, m and m^+ correspond to anomalous Green's functions. The representation phase space is therefore $\vec{\lambda} = (\Omega, \boldsymbol{\alpha}, \boldsymbol{\beta}, n, m, m^+)$ for bosons; in the case of fermions, one must set $\boldsymbol{\alpha} = \boldsymbol{\beta} = 0$.

The significance of the definition of n and m is that it leads to useful bosonic and fermionic operator identities. For example, one finds that

$$\langle \hat{a}_i^\dagger \hat{a}_j \rangle = \langle \beta_i \alpha_j + n_{ij} \rangle_P, \quad (12)$$

where the weighted average is defined as

$$\langle \hat{O} \rangle = \langle O(\vec{\lambda}) \rangle_P = \int O(\vec{\lambda}) \Omega P(\vec{\lambda}, \tau) d\vec{\lambda}. \quad (13)$$

For representations with fixed n_{ij} , one thus obtains a generalized operator-ordering. Classical phase-space distributions are recovered on setting $\alpha_i = \beta_i^*$, and $n_{ij} = c\delta_{ij}$. For example, the Glauber-Sudarshan P -representa-

tion has $c = 0$, while the Wigner distribution has $c = -1/2$. More generally, this type of phase space allows for a stochastic covariance, which can dynamically change in time and space to suit the physical system.

Other useful identities involve the relationship between the action of operators on the kernel, and the corresponding differential operators acting on the distribution itself. For simplicity, these are given in the number-conserving case ($\boldsymbol{\alpha} = \boldsymbol{\beta} = 0, m = 0, m^+ = 0$):

$$\begin{aligned} \hat{n} \hat{\Lambda} &\longrightarrow nP - (I \pm n) \frac{\overleftrightarrow{\partial}}{\partial n} nP, \\ \hat{\Lambda} \hat{n} &\longrightarrow nP - n \frac{\overleftrightarrow{\partial}}{\partial n} (I \pm n)P, \end{aligned} \quad (14)$$

where $(\overleftrightarrow{\partial}/\partial n)_{ij} \equiv \overleftrightarrow{\partial}/\partial n_{ji}$ is a differential operator that acts both to the left and the right.

Evolution Equations

There are three main types of problems studied with this approach, which provides a unified method for interacting fermions and bosons:

Canonical ensembles—thermal initial conditions.

Quantum dynamics—unitary nonlinear time-evolution.

Master equations—open system time-evolution to a steady-state.

The purpose of the phase-space representation is to transform exponentially complex operator equations into tractable phase-space equations, which can then be effectively sampled via probabilistic means. For example, suppose that we wish to calculate a thermal ensemble. The grand-canonical density operator can be written as an operator differential equation,

$$\frac{d\hat{\rho}}{dt} = -\frac{1}{2} [\hat{H} - \mu \hat{N}, \hat{\rho}]_+ = \hat{L}[\hat{\rho}]. \quad (15)$$

Similarly, one can also treat unitary evolution or evolution under a master equation as a generalized Liouville operator. By making use of the operator identities above, and provided conditions of compactness that allow partial integration are satisfied, one can transform the exponentially large operator equation into a stochastic equations that can be treated either numerically or, in some cases, even analytically. The generic form that results, in the Ito calculus, is:

$$\begin{aligned} d\Omega/\partial t &= \Omega[U + \mathbf{g}\boldsymbol{\zeta}], \\ d\boldsymbol{\lambda}/\partial t &= A + B(\boldsymbol{\zeta} - \mathbf{g}), \end{aligned} \quad (16)$$

where $\boldsymbol{\zeta}$ is a vector of Gaussian white noises. The function \mathbf{g} is a ‘‘stochastic gauge’’ function, that can be adjusted to guarantee the stability of the resulting drift equations.

In summary, this method greatly extends the approaches of Glauber, Sudarshan, Husimi and Wigner.

No approximations are needed, apart from the sampling error, which can be estimated and reduced by using more samples. The representations use positive, nonsingular distributions on a relatively small (non-exponential) phase space. This reduces the overall complexity enormously. The price that is paid is that many trajectories can be needed to control sampling error, which typically grows with time. One must also design an appropriate stabilizing gauge \mathbf{g} , as stable trajectories are essential to remove boundary terms. The overall procedure is outlined schematically in Fig. 2.

BOSONS

The simplest general model of an interacting Bose gas is the Bose–Hubbard model, which includes nonlinear interactions at each site, together with linear interactions coupling different sites:

$$\hat{H}(\mathbf{a}, \mathbf{a}^\dagger) = \hbar[\sum \sum \omega_{ij} a_i^\dagger a_j + \sum : \hat{n}_j^2 :], \quad (17)$$

where the frequency term ω_{ij} is a nonlocal coupling, which includes chemical potential. The boson number operator is $\hat{n}_i = a_i^\dagger a_i$. The most commonly used technique here is the positive- P representation, although more general Gaussian methods are also possible.

Single-Mode Phase-Diffusion

As an example, consider the case of a single potential well containing a BEC in an initial coherent state. After applying the relevant operator mappings, one obtains the following time-evolution equations:

$$\begin{aligned} i \frac{d\alpha}{d\tau} &= [\text{Re}[\beta\alpha] + \omega + \sqrt{i}\zeta_1(\tau)]\alpha, \\ -i \frac{d\beta}{d\tau} &= [\text{Re}[\beta\alpha] + \omega + \sqrt{-i}\zeta_2(\tau)]\beta, \\ \frac{d\Omega}{d\tau} &= \Omega[g_1\zeta_1(\tau) + g_2\zeta_2(\tau)]. \end{aligned} \quad (18)$$

Here, unitary evolution leads to nonlinear phase-diffusion, as has been experimentally observed [34]. The stochastic technique can be utilized to carry out a simulation of quantum evolution of an initial coherent state of up to 10^{23} bosons!

This is shown in Fig. 3, where first 100 atoms, and then 10^{23} atoms were simulated after appropriate choices of gauges $g_{1,2}$ and noises $\zeta_{1,2}$ [35]. A time-reversal test of unitary evolution was carried out by reversing the sign of the Hamiltonian, in order to observe a recurrence to the initial physical state. This is even possible experimentally, using Feshbach resonances to control the interaction.

The distribution graphs in Fig. 4 demonstrate that the mechanism for the recurrence is not through a recurrence of the entire distribution, as only the physically observable moments have to show recurrence.

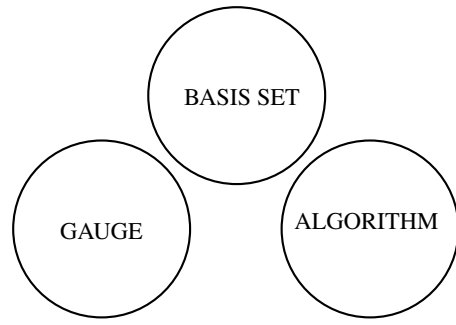


Fig. 2. Strategies that need to be considered and optimized in quantum simulations.

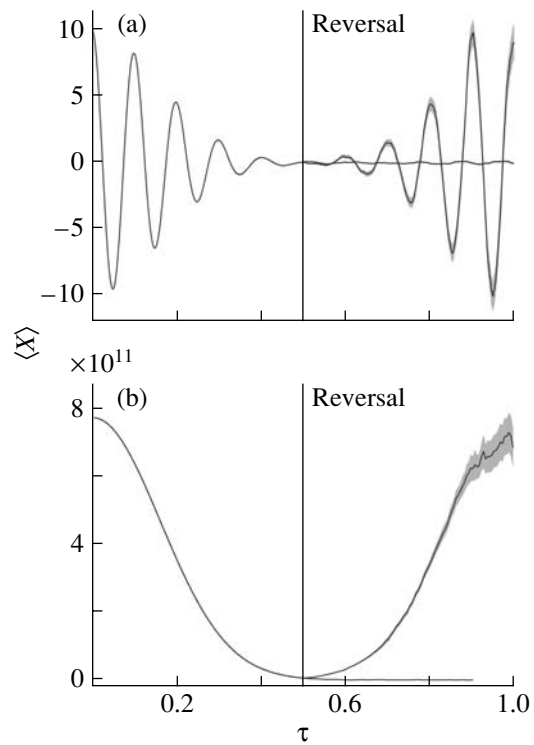


Fig. 3. Simulation of (a) 100 and (b) 10^{23} atoms in a single-mode trap, showing phase-decay together with a recurrence due to time-reversal.

The non-uniqueness of the basis means that the final distribution is actually *different* to the initial one; the effect of time-reversal is to change the detailed structure of the diffusive broadening, so that the final and initial distributions have an equivalent physical density matrix.

Optical Fibre Squeezing Experiment

To a very good approximation, photons in an optical fiber, with the Kerr nonlinearity present, are an experi-

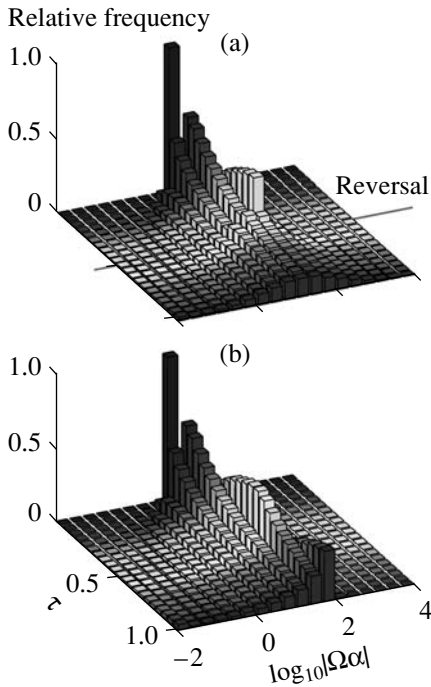


Fig. 4. Phase-space distribution in the single-mode trap simulations with $N = 100$ showing (a) time-reversal, (b) no time-reversal.

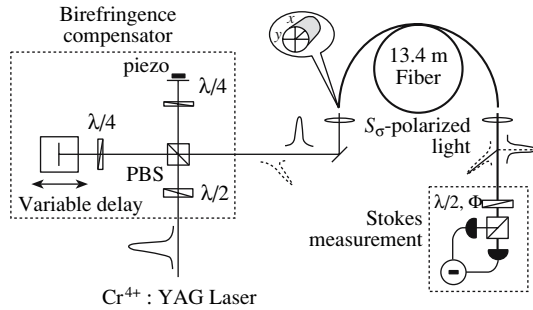


Fig. 5. Polarization-squeezing experiment [38].

mental implementation of the famous one-dimensional Bose gas model in quantum field theory [36, 37]. Phase-space methods were used to make first-principles, testable predictions of quantum squeezing in this environment. We will show that these results are in excellent quantitative agreement with experiment, even including dissipation.

We focus on recent polarization squeezing experiments [38], which are an efficient and flexible method for generating quantum states in the fiber [14]. The experimental set-up is illustrated in Fig. 5. Pulses are generated in pairs and propagate down orthogonal polarization modes of an optical fiber. They are then combined in a Stokes measurement of polarization squeezing by means of a polarization rotator, a beam splitter and two detectors.

Because the experiment involves ultrashort pulses, the quantum description must use photon-density operators $\hat{\Psi}_x(t, z)$ and $\hat{\Psi}_y(t, z)$ that include a range of spectral components:

$$\hat{\Psi}_\sigma(t, z) \equiv \frac{1}{\sqrt{2\pi}} \int dk \hat{a}_\sigma(t, k) e^{i(k-k_0)z + i\omega_0 t}, \quad (19)$$

where $\sigma = x, y$. The commutation relations of these operators are $[\hat{\Psi}_\sigma(t, z), \hat{\Psi}_{\sigma'}^\dagger(t, z')] = \delta(z - z')\delta_{\sigma\sigma'}$.

For convenience, we use scaled variables in propagative frame: $\tau \equiv (t - z/v)$, $\zeta \equiv z/z_0$ and $\hat{\phi}_\sigma \equiv \hat{\Psi}_\sigma \sqrt{vt_0/\bar{n}}$, where t_0 is the pulse duration, $z_0 \equiv t_0^2/|k''|$ is the dispersion length and $2\bar{n} \equiv 2|k''|Ac/(n_2\hbar\omega_c^2 t_0)$ is the photon number in a soliton pulse.

To describe the evolution of the photon flux $\hat{\phi}_\sigma(\tau, \zeta)$, we employ a quantum model of a radiation field propagating along a silica fiber, including $\chi^{(3)}$ nonlinear responses of the material and non-resonant coupling to phonons [39, 40]. The phonons provide a non-Markovian reservoir that generates additional, delayed nonlinearity, as well as spontaneous and thermal noise. Because of fiber birefringence, the two polarization components do not temporally overlap for most of the fiber length, and so the cross-polarization component of the Raman gain is neglected. The result, after discretization, is a Hubbard model like Eq. (17), except with additional coupling to phonon reservoirs.

The quantum operator equations are obtained by integration of the Heisenberg equations for the phonon operators to derive quantum Langevin equations for the photon-flux field:

$$\begin{aligned} \frac{\partial}{\partial \zeta} \hat{\phi}_\sigma(\tau, \zeta) &= \frac{i}{2} \frac{\partial^2}{\partial \tau^2} \hat{\phi}_\sigma(\tau, \zeta) + i\hat{\Gamma}_\sigma(\tau, \zeta) \hat{\phi}_\sigma(\tau, \zeta) \\ &+ i \int_{-\infty}^{\infty} d\tau' h(\tau - \tau') \hat{\phi}_\sigma^\dagger(\tau', \zeta) \hat{\phi}_\sigma(\tau', \zeta) \hat{\phi}_\sigma(\tau, \zeta), \end{aligned} \quad (20)$$

where the nonlinear response function $h(\tau)$ includes contributions from both the instantaneous electronic response and the Raman response determined by the gain function $\alpha^R(\omega)$ [39, 41, 42]. The correlations of the reservoir fields are

$$\begin{aligned} &\langle \hat{\Gamma}_\sigma^\dagger(\omega', \zeta') \hat{\Gamma}_\sigma(\omega, \zeta) \rangle \\ &= \frac{\alpha^R(|\omega|)}{\bar{n}} [n_{\text{th}}(|\omega|) + \Theta(-\omega)] \delta(\zeta - \zeta') \delta(\omega - \omega') \delta_{\sigma\sigma'}, \end{aligned} \quad (21)$$

where n_{th} is the temperature-dependent Bose distribution of phonon occupations. The Stokes ($\omega < 0$) and anti-Stokes ($\omega > 0$) contributions to the Raman noise are included by means of the Heaviside step function Θ .

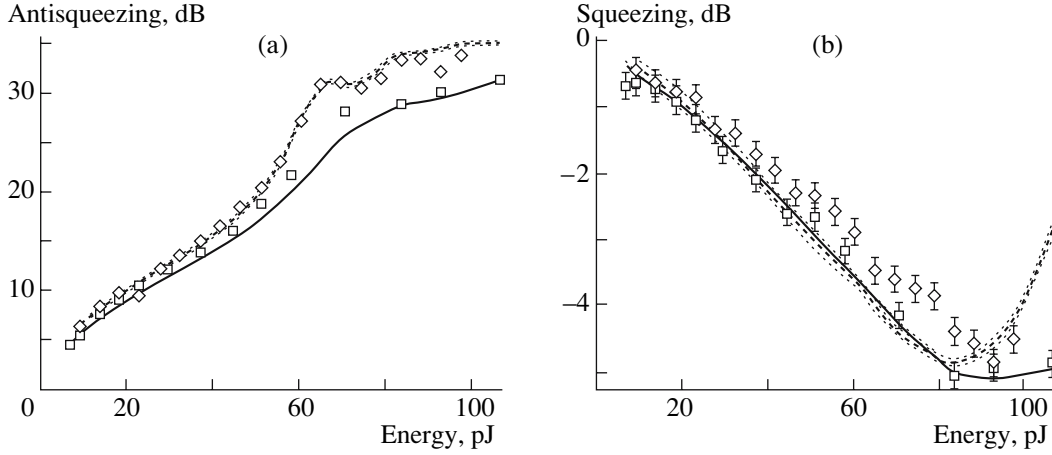


Fig. 6. Antisqueezing (a) and squeezing (b) for $L_1 = 13.4$ m (squares) and $L_2 = 30$ m (diamonds) fibres. Solid and dashed lines show the simulation results for $L_1 = 13.4$ m and $L_2 = 30$ m, respectively. Dotted lines indicate sampling error in simulation results. Simulations are adjusted for linear loss of 24% and low-frequency GAWBS noise, which mainly affects the squeezing only at low power. Parameters are: $t_0 = 74$ fs, $z_0 = 0.52$ m, $\bar{n} = 2 \times 10^8$, $E_s = 54$ pJ, and $\lambda_0 = 1.51$ μ m.

In all, we have over 10^8 photons in more than 10^2 modes, corresponding to an enormously large Hilbert space. Quantum dynamical simulations of such systems have been performed exactly using the $+P$ representation [36, 43]. However, for large photon number \bar{n} and short propagation distance L , these exact squeezing predictions agree with a truncated Wigner phase-space method [44], which allows faster calculations. In effect, the Wigner representation maps a field operator to a stochastic field: $\hat{\phi}_\sigma(\zeta, \tau) \rightarrow \phi_\sigma(\zeta, \tau)$. Stochastic averages involving this field then correspond to symmetrically ordered correlations of the quantum system. Because of the symmetric-ordering correspondence, quantum effects enter via vacuum noise.

After the mapping, we obtain a Raman-modified stochastic nonlinear Schrödinger equation for the photon flux that is of exactly the same form as Eq. (20) [39, 45]. The correlations of the Raman noise fields Γ_σ and the initial vacuum noise are, respectively,

$$\begin{aligned} & \langle \Gamma_\sigma(\omega, \zeta) \Gamma_\sigma(\omega', \zeta') \rangle \\ &= \frac{\alpha^R(|\omega|)}{\bar{n}} \left[n_{\text{th}}(|\omega|) + \frac{1}{2} \right] \delta(\zeta - \zeta') \delta(\omega - \omega') \delta_{\sigma\sigma'}, \quad (22) \end{aligned}$$

$$\langle \Delta\phi_\sigma(\tau, 0) \Delta\phi_\sigma^*(\tau', 0) \rangle = (1/2\bar{n}) \delta(\tau - \tau') \delta_{\sigma\sigma'}.$$

Because of the symmetrically ordered mapping, the Stokes and anti-Stokes contributions to the Wigner-Raman noise are identical.

Antisqueezing and squeezing results are shown in Fig. 6, for 13.4 m and 30 m of fiber, with and without the excess phase noise included. The theoretical results for both squeezing and antisqueezing closely match the experimental data. The results also show a deterioration of squeezing at higher intensity due to Raman effects, especially for longer fiber lengths.

BEC Collision with 150000 Atoms from First Principles

The collision of pure ^{23}Na BECs, as in a recent experiment at MIT [46], represents another opportunity for observational tests of first-principles quantum dynamical simulations [15, 47]. In the simulations, a 1.5×10^6 atom condensate is prepared in a cigar-shaped magnetic trap with frequencies 20 Hz axially in the “X” direction, and 80 Hz radially (“Y” and “Z”). A brief Bragg laser pulse coherently imparts an X velocity of $2v_Q \approx 20$ mm/s to half of the atoms, which is much greater than the sound velocity of 3.1 mm/s. Another much weaker pulse generates a small 2% “seed” wavepacket at a Y velocity of $v_s = 9.37$ mm/s relative to the center of mass.

At this point the trap is turned off so that the wavepackets collide freely. In a center-of-mass frame, atoms are scattered preferentially into a spherical shell in momentum space with mean velocities $v_s \approx v_Q$. Simultaneously, a four-wave mixing process generates a new coherent wavepacket at Y velocity $-v_s$, as well as growing the strength of both of the wavepackets at $\pm v_s$ by Bose enhanced scattering.

The dynamics of the distribution of atom velocities and correlations between the scattered atoms have been calculated and are shown in Figs. 7 and 8. Such correlations have recently become experimentally measurable [48–50], and correlation behavior qualitatively similar to that predicted by this model have been seen [51]. The system is described by

$$\hat{H} = \int \left[\frac{\hbar^2}{2m} \nabla \hat{\Psi}^\dagger \nabla \hat{\Psi} + \frac{g}{2} \hat{\Psi}^{\dagger 2} \hat{\Psi}^2 \right] d^3 \vec{x}. \quad (23)$$

The simulation is carried out using the positive- P representation in the center-of-mass frame from the

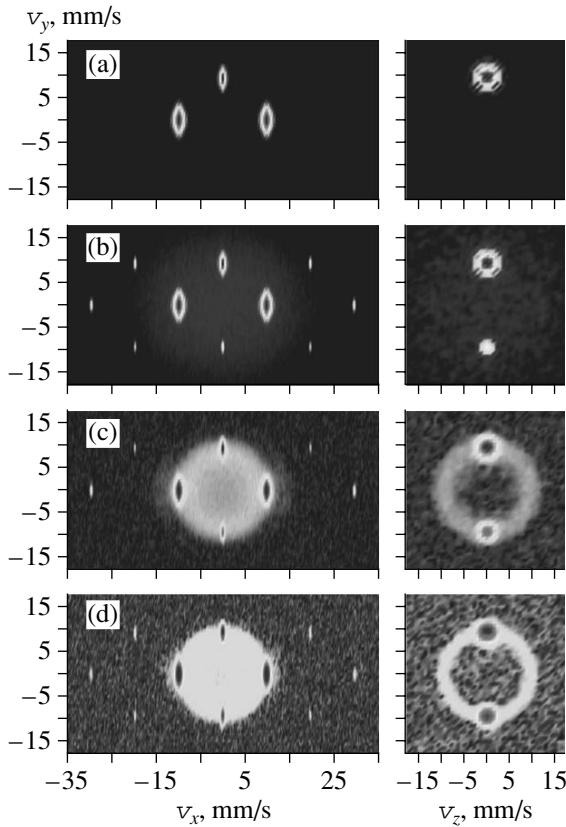


Fig. 7. Momentum space snap-shots in the center-of-mass frame $t = 0$ (a), 32 (b), 189 (c), 411 μs (d). *Left:* Velocity distributions in the axial (x) and radial (y) directions. *Right:* Radial distribution at $x = 0$. The formation of the fourth coherent wavepacket at $v_y \approx -v_s$ and the scattered shell at $|v| \approx v_s = 9.37$ mm/s are seen. Logarithmic color scale. Average of 1492 trajectories.

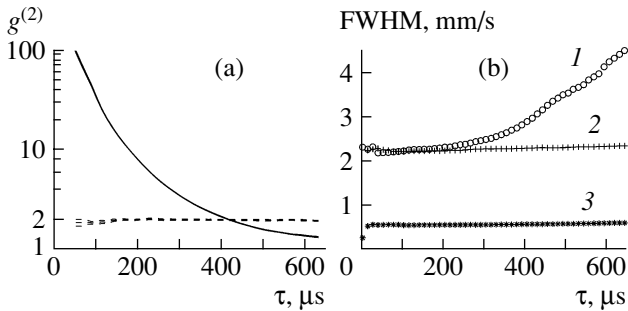


Fig. 8. Correlations between scattered atoms: time evolution. Plate (a) shows the extremely strong number correlations $g^{(2)}(v_0, -v_0)$ between atoms with opposite velocity (solid line) in the scattered shell at $|v_0| = v_s$ (away from the coherent wavepackets), and thermal correlations $g^{(2)}(v_0, v_0) = 2$ between scattered atoms at the same velocity (dashed). Triple lines indicate uncertainty. Plate (b) shows the coherence width in velocity space for scattered atoms at similar velocities centered around v_0 : 1—in radial direction, 2—intangential direction, 3—in axial (x) direction. Plotted is the full-width at half-maximum (FWHM) of $|g^{(1)}(v_0, v_0 + v)|$.

moment the lasers and trap are turned off ($t = 0$). The initial wavefunction is modeled as the coherent-state mean-field Gross–Pitaevskii (GP) solution of the trapped $t < 0$ condensate, but modulated with a factor

$$[\sqrt{0.49}e^{imv_0x/\hbar} + \sqrt{0.49}e^{-imv_0x/\hbar} + \sqrt{0.02}e^{-imv_s y/\hbar}],$$

which imparts the initial velocities. The field Hamiltonian is discretized with a lattice size of $432 \times 105 \times 50$, again generating a Hubbard-type Hamiltonian like Eq. (17).

As one might expect of a method that attacks such an exponentially complex problem, there are limitations. Most significantly, the size of the sampling uncertainty grows with time, and eventually reaches a size where it is no longer practical to produce enough trajectories to get useful precision. In the above case a useful observable-to-noise ratio lasted until $t \approx 410$ μs . In general the simulation time possible depends on several factors: coarser lattices, weaker interactions, or smaller density all extend it. This time can be estimated using the formulae found in [52]. Comparisons were made with a previous approximate simulation [53], using a truncated Wigner method [4, 44]. The approximate method was less accurate at large momentum cutoff, due to a diverging truncation error.

The model treats $M = 2.268 \times 10^6$ interacting momentum modes. Since each of the $N = 1.5 \times 10^5$ atoms can be in any one of the modes, the Hilbert space contains about $N_s \approx M^N \approx 10^{1000000}$ orthogonal quantum states. In terms of accessible states at fixed number, there are $N_s \approx (M/N)^N \approx 2^{600000}$ states, or 600000 qubits.

This is the largest Hilbert space ever treated in a first-principles quantum dynamical simulation.

FERMIONS

Hubbard Model

To demonstrate the utility of this fermionic representation, we next consider the *fermionic* Hubbard model [54]. This is well-known in condensed matter physics as the simplest model of interacting fermions on a lattice:

$$\hat{H}(\hat{n}_\downarrow, \hat{n}_\uparrow) = - \sum_{ij, \sigma} t_{ij} \hat{n}_{ij, \sigma} + U \sum_j : \hat{n}_{j, j, \downarrow} \hat{n}_{j, j, \uparrow} : . \quad (24)$$

Here $\hat{n}_{ij, \sigma} \equiv \hat{a}_{i, \sigma}^\dagger \hat{a}_{j, \sigma}$, for lattice index j and spin index $\sigma = (\uparrow, \downarrow) = (-1, 1)$, while t_{ij} is the inter-site coupling and U is the strength of on-site interaction between particles.

Thought to be relevant to high- T_c superconductors [55], the Hubbard model has had renewed interest because it describes an ultra-cold gas in an optical lattice [56], as has been experimentally realized by Köhl et al. [57]. Within this simple model is a great complex-

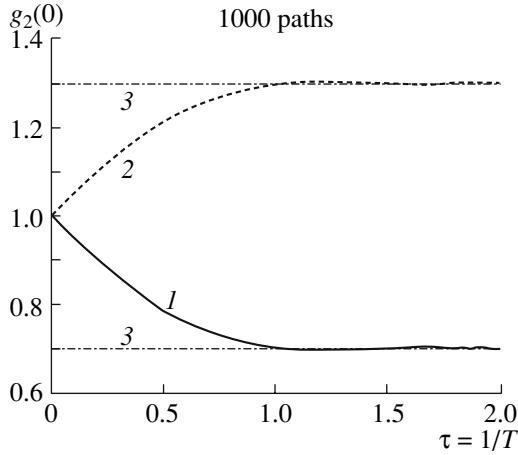


Fig. 9. 1D Hubbard model: Correlation function $\langle n_{\downarrow} n_{\uparrow} \rangle$ versus temperature. The 100-site numerical solution (1—repulsive, 2—attractive) is compared with the zero-temperature exact solution (3) of an infinite lattice [60]: $t = 1$ and $U = 2$.

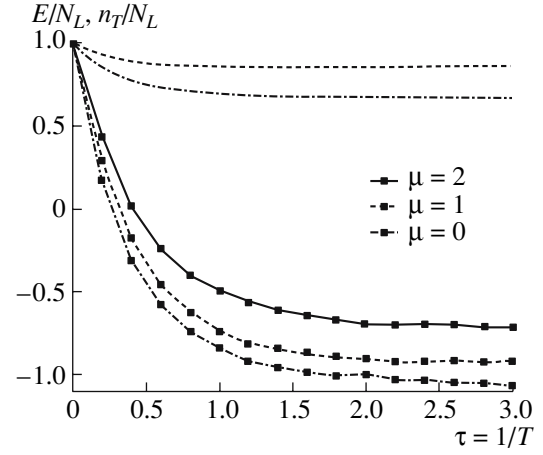


Fig. 10. 2D Hubbard model on a 16×16 lattice: Energy as a function of temperature for various chemical potentials. $t = 1$ and $U = 4$.

ity, that leads to sampling error problems for quantum Monte Carlo (QMC) methods because of negative weights [58]. Such sign problems occur for repulsive interactions away from half-filling in two or more dimensions, and increase with lattice size and interaction strength [59].

Results of recent phase-space numerical simulations [25] in one and two dimensions are shown in Figs. 9 and 10. The sampling error remains well-controlled at low temperatures, even for filling factors in 2D for which other QMC methods suffer sign problems.

To explain the method used, we first note that the Hubbard Hamiltonian conserves number, so the number-conserving subset of Gaussian operators provides a complete basis, i.e., the anomalous variables remain zero. The mappings given above can be applied to the grand canonical equilibrium equation to give the Ito phase-space equations [13]:

$$dn_{\sigma}/d\tau = (1/2)\{(I - n_{\sigma})T_{\sigma}^{(1)}n_{\sigma} + n_{\sigma}T_{\sigma}^{(2)}(I - n_{\sigma})\}. \quad (25)$$

The propagation matrices are defined for $U > 0$, as

$$T_{i,j,\sigma}^{(r)} = t_{ij} - \delta_{i,j}\{Un_{j,j,-\sigma} - \mu + \sigma\xi_j^{(r)}\}, \quad (26)$$

where the stochastic terms are Gaussian white noises with the correlations

$$\langle \xi_j^{(r)}(\tau)\xi_{j'}^{(r')}(\tau') \rangle = 2U\delta(\tau - \tau')\delta_{j,j'}\delta_{r,r'}. \quad (27)$$

Associated with each stochastic path is a weight, governed by $d\Omega/d\tau = -\Omega H(n_1, n_{-1})$. Importantly, because the choice of mapping, the phase-space equations are real and the weights thus remain positive, avoiding the usual manifestation of the sign problem.

More precise numerical simulations by Assaad et al. [61] have revealed that there is difficulty in sampling

ground state properties with these phase-space equations. However, they also show that the correct ground-state results can be obtained by supplementing the phase-space simulations with a symmetry projection procedure.

Finally, we remark that the mapping from the Hubbard model to phase-space equation is far from unique. Thus these phase-space simulations of the Hubbard model may well be improved by appropriate choice of basis subset and stochastic gauge, as for bosonic simulations.

SUMMARY

In summary, coherence theory and coherent-state methods leads to a unified phase-space representation for bosonic and fermionic quantum many-body systems, which are useful in simulations both in real time and in inverse temperature. Calculations have been carried out in one, two and three dimensions, with up to 10^{23} particles and 10^6 modes. This is equivalent to a Hilbert space of nearly a million qubits. Phase-space ideas are also applicable to other complex systems [62, 63]—ranging from genetics, astrophysics, and biochemistry, to condensed matter, particle physics and possibly even molecular physics.

ACKNOWLEDGMENTS

We acknowledge funding from the Australian Research Council and useful discussions with K.V. Kheruntsyan.

REFERENCES

1. E. Schrödinger, *Naturwiss.* **14**, 664 (1926).
2. E. C. G. Sudarshan, *Phys. Rev. Lett.* **10**, 277 (1963).
3. R. J. Glauber, *Phys. Rev.* **131**, 2766 (1963).

4. E. P. Wigner, Phys. Rev. **40**, 749 (1932).
5. K. Husimi, Phys. Math. Soc. Jpn. **22**, 264 (1940).
6. M. Lax, Phys. Rev. **145**, 110 (1966).
7. G. S. Agarwal and E. Wolf, Phys. Rev. D **2**, 2161 (1970).
8. G. S. Agarwal and E. Wolf, Phys. Rev. D **2**, 2187 (1970).
9. S. Chaturvedi, P. Drummond, and D. F. Walls, J. Phys. A **10**, L187 (1977).
10. P. D. Drummond and C. W. Gardiner, J. Phys. A **13**, 2353 (1980).
11. P. Deuar and P. D. Drummond, Phys. Rev. A **66**, 33812 (2002).
12. J. F. Corney and P. D. Drummond, Phys. Rev. A **68**, 63822 (2003).
13. J. F. Corney and P. D. Drummond, Phys. Rev. B **73**, 125112 (2006).
14. J. F. Corney, P. D. Drummond, J. Heersink, et al., Phys. Rev. Lett. **97**, 023606 (2006).
15. P. Deuar and P. D. Drummond, arXiv: cond-mat/0607831.
16. U. V. Poulsen and K. Mølmer, Phys. Rev. A **64**, 013616 (2001).
17. J. J. Hope and M. K. Olsen, Phys. Rev. Lett. **86**, 3220 (2001).
18. U. V. Poulsen and K. Mølmer, Phys. Rev. A **63**, 023604 (2001).
19. K. V. Kheruntsyan and P. D. Drummond, Phys. Rev. A **66**, 031602(R) (2002).
20. C. M. Savage, P. E. Schwenn, and K. V. Kheruntsyan, arXiv: cond-mat/0606345; Phys. Rev. A (in press).
21. K. V. Kheruntsyan, M. K. Olsen, and P. D. Drummond, Phys. Rev. Lett. **95**, 150405 (2005).
22. M. K. Olsen, A. B. Melo, K. Dechoum, and A. Z. Khouiry, Phys. Rev. A **70**, 043815 (2004).
23. M. K. Olsen, A. S. Bradley, and M. D. Reid, J. Phys. B **39** (2006).
24. P. D. Drummond and K. Dechoum, Phys. Rev. Lett. **95**, 083601 (2005).
25. J. F. Corney and P. D. Drummond, Phys. Rev. Lett. **93**, 260401 (2004).
26. U. Schollwöck, Rev. Mod. Phys. **77**, 259 (2005).
27. W. Kohn, Rev. Mod. Phys. **71**, 1253 (1999).
28. J. L. Martin, Proc. Roy. Soc. (London) A **251**, 543 (1959).
29. Y. Ohnuki and T. Kashiwa, Prog. Theor. Phys. **60**, 548 (1978).
30. J. W. Negele and H. Orland, *Quantum Theory of Many-Particle Systems* (Perseus Publications, Cambridge, 1989).
31. K. E. Cahill and R. J. Glauber, Phys. Rev. A **59**, 1538 (1999).
32. L. I. Plimak, M. J. Collett, and M. K. Olsen, Phys. Rev. A **64**, 063409 (2001).
33. J. F. Corney and P. D. Drummond, J. Phys. A **39**, 269 (2006).
34. M. Greiner, O. Mandel, T. W. Hansch, and I. Bloch, Nature **419**, 51 (2002).
35. M. R. Dowling, P. D. Drummond, M. J. Davis, and P. Deuar, Phys. Rev. Lett. **94**, 130401 (2005).
36. P. D. Drummond and S. J. Carter, J. Opt. Soc. Am. B **4**, 1565 (1987).
37. B. Yurke and M. J. Potasek, J. Opt. Soc. Am. B **6**, 1226 (1989).
38. J. Heersink, V. Josse, G. Leuchs, and U. L. Andersen, Opt. Lett. **30**, 1192 (2005).
39. P. D. Drummond and J. F. Corney, J. Opt. Soc. Am. B **18**, 139 (2001).
40. S. J. Carter and P. D. Drummond, Phys. Rev. Lett. **67**, 3757 (1991).
41. R. H. Stolen, C. Lee, and R. K. Jain, J. Opt. Soc. Am. B **1**, 652 (1984).
42. R. H. Stolen, J. P. Gordon, W. J. Tomlinson, and H. A. Haus, J. Opt. Soc. Am. B **6**, 1159 (1989).
43. S. J. Carter, P. D. Drummond, M. D. Reid, and R. M. Shelby, Phys. Rev. Lett. **58**, 1841 (1987).
44. P. D. Drummond and A. D. Hardman, EuroPhys. Lett. **21**, 279 (1993).
45. S. J. Carter, Phys. Rev. A **51**, 3274 (1995).
46. J. M. Vogels, K. Xu, and W. Ketterle, Phys. Rev. Lett. **89**, 020401 (2002).
47. P. Deuar, Ph. D. Thesis, The University of Queensland; arXiv: cond-mat/0507023.
48. M. Greiner, C. A. Regal, J. T. Stewart, and D. S. Jin, Phys. Rev. Lett. **94**, 110401 (2005).
49. S. Fölling, F. Gerbier, A. Widera, et al., Nature **434**, 481 (2005).
50. M. Schellekens, R. Hoppeler, A. Perrin, et al., Science **310**, 648 (2005).
51. C. I. Westbrook, private communication.
52. P. Deuar and P. D. Drummond, J. Phys. A **39**, 1163 (2006).
53. A. A. Norrie, R. J. Ballagh, and C. W. Gardiner, Phys. Rev. Lett. **94**, 040401 (2005).
54. J. Hubbard, Proc. R. Soc. (London) A **276**, 238 (1963).
55. J. R. Schrieffer, *Theory of Superconductivity* (Benjamin, Massachusetts, 1964).
56. W. Hofstetter, J. I. Cirac, P. Zoller, et al., Phys. Rev. Lett. **89**, 220407 (2002).
57. M. Kohl, J. Moritz, T. Stoferle, et al., Phys. Rev. Lett. **94**, 080403 (2005).
58. W. von der Linden, Phys. Rep. **220**, 53 (1992).
59. R. R. dos Santos, Brazilian J. Phys. **33**, 36 (2003).
60. E. H. Lieb and F. Y. Wu, Phys. Rev. Lett. **20**, 1445 (1968).
61. F. F. Assaad, P. Werner, P. Corboz, et al., Phys. Rev. B **72**, 224518 (2005).
62. C. W. Gardiner and S. Chaturvedi, J. Stat. Phys. **17**, 429 (1977).
63. P. D. Drummond, Eur. Phys. J. B **38**, 617 (2004).